

Jan Valášek; Petr Sváček

Simplified mathematical models of fluid-structure-acoustic interaction problem motivated by human phonation process

In: Jan Chleboun and Jan Papež and Karel Segeth and Jakub Šístek and Tomáš Vejchodský (eds.): Programs and Algorithms of Numerical Mathematics, Proceedings of Seminar. Hejnice, June 23-28, 2024. , Prague, 2025. pp. 169–187.

Persistent URL: <http://dml.cz/dmlcz/703230>

Terms of use:

Institute of Mathematics of the Czech Academy of Sciences provides access to digitized documents strictly for personal use. Each copy of any part of this document must contain these *Terms of use*.



This document has been digitized, optimized for electronic delivery and stamped with digital signature within the project *DML-CZ: The Czech Digital Mathematics Library*
<http://dml.cz>

SIMPLIFIED MATHEMATICAL MODELS OF FLUID-STRUCTURE-ACOUSTIC INTERACTION PROBLEM MOTIVATED BY HUMAN PHONATION PROCESS

Jan Valášek^{1,2}, Petr Sváček²

¹ Institute of Mathematics, Czech Academy of Sciences
Žitná 25, 115 67 Praha 1, Czech Republic
valasek@math.cas.cz

² Faculty of Mechanical Engineering, CTU in Prague
Karlovo nám. 13, Praha 2, 121 35, Czech Republic
petr.svacek@fs.cvut.cz

Abstract: Human phonation process represents an interesting and complex problem of fluid-structure-acoustic interaction, where the deformation of the vocal folds (elastic body) are interplaying with the fluid flow (air stream) and the acoustics. Due to its high complexity, two simplified mathematical models are described – the fluid-structure interaction (FSI) problem describing the self-induced vibrations of the vocal folds, and the fluid-structure-acoustic interaction (FSAI) problem, which also involves aeroacoustic phenomena. The FSI model is based on the incompressible Navier-Stokes equations in the ALE formulation coupled with the linear elasticity model. Both the fluid and structural models are approximated using finite element methods, and the influence of different inlet boundary conditions is discussed in detail. For the FSAI model, an aeroacoustic hybrid approach is used, incorporating the Lighthill analogy or the perturbed convective wave equation. The acoustic results strongly depend on the proper choice of the computational acoustic domain (i.e. vocal tract model). Further, the spatial and frequency distributions of sound sources computed from the FSI solution are compared for both used approaches. The final frequency spectra of acoustic pressure at the mouth position are also analyzed for both approaches.

Keywords: human phonation, flow-induced vibrations, Navier-Stokes equations, aeroacoustic analogy, flutter instability, finite element method.

MSC: 65M60, 74F10, 76Q05.

1. Introduction

The basic sound of human phonation is created by an airstream (fluid flow) pouring through a channel constricted by vibrating elastic vocal folds (VFs), naturally

leading to fluid-structure interaction (FSI) problem, see [17]. Moreover, both the involved physical fields also interact with the acoustic field and we speak in general about fluid-structure-acoustic interaction (FSAI) problem, [7, 15], see Figure 1. The acoustic interaction occurs in two primary ways: the resonant frequencies of the acoustic domain dominate the output signal as other frequencies are less distinct, [17, 14], and acoustic waves can influence VF vibration patterns (as the major sound source mechanism). This can occur particularly under high sound pressure levels (SPL), as observed in loud singing [23], or during phonation into a length-adjusted tube used in voice therapy [4].

In this paper the modelling of human phonation during the normal speech is considered, where the source-filter theory ([17, 14]) can be utilized (due to low acoustic SPL) neglecting any acoustic influence on the VF vibration. This allows us to decouple the acoustic problem from the FSI problem and to use the hybrid approach of aeroacoustic analogies, see Figure 1 on the right. The acoustic problem, treated as a post-processing task after the FSI simulation, can be solved with a different solver, offering many advantages, see [7]. This simplified FSAI model, [13], is the primary focus here.

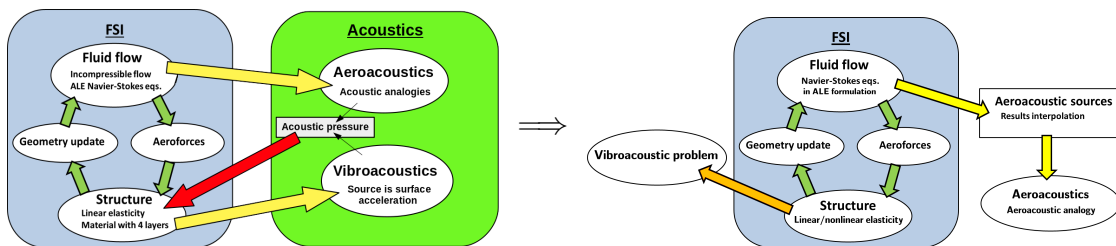


Figure 1: Dependence of physical fields in FSAI problem and its possible simplification, where the acoustic influence on the FSI problem is neglected.

Another mechanism of sound production, aside from the aeroacoustic one, is the vibrations of VFs, see e.g. [7]. This contribution is often modelled as a simplified vibro-acoustic problem, neglecting the influence of the acoustic field on VF vibration, see Fig. 1 right. This problem is sometimes overlooked due to anticipated prominence of aerodynamically produced sound, [13], for a more detailed discussion see e.g. [23].

The typical healthy VF vibration regime is characterized by flutter instability, making modelling and numerical approaches highly demanding, [17], [15]. During the flutter regime the structural displacements exponentially grow until – for the case of healthy phonation – the both VFs reach contact and impact each other. Mathematical modelling of contact problems is challenging on its own and highly demanding to be included in the already complex FSAI problem [13]. Although some promising results emerged, e.g. a low-order model comprising a three-mass system coupled with 1D Euler equations and Hertz contact theory applied, [5], or more recently a simplified contact treatment in the continuum settings [20], the contact modelling is completely omitted here. On the other hand, the novelty of the

present study lies in the detailed analysis of the energy balance between the flow and the structure based on the pressure-gap curve [4], as well as in the improved acoustic results compared to those previously published in [18], where the final results were affected by the improper implementation of a perfectly matched layer (PML).

The FSI problem is modelled here by a linear elasticity model for the vocal folds and the incompressible Navier-Stokes equations for the air flow. The arbitrary Lagrangian-Eulerian (ALE) method addresses the time-dependent fluid domain, see [2], offering simplicity in description and implementation, [16], but requiring remeshing or additional modifications for topological changes, such as the omitted contact phenomenon, [8, 20]. The numerical discretization by the finite element method (FEM) is performed and the stabilization of the convection-dominated airflow is applied. Finally, two aeroacoustic approaches are presented: the classical Lighthill (LH) analogy and the perturbed convective wave equation (PCWE) based on a careful separation of acoustic from other fluid components, [1, 7]. The analysis of computed sound sources is important for validating the computation procedure and identifying the origin and location of the generated sound, [13]. Subsequently, the time propagation problem is solved in the selected acoustic domain representing vocal tract geometry, which can strongly influence acoustic results, cf. [23] and [13]. The PML technique models acoustically open boundaries by effectively absorbing outgoing acoustic waves, surpassing other methods limited to specific angles, [7].

The structure of the paper is as follows. The next section is devoted to the FSI problem formulation including also description of numerical approximation and details of the FSI simulation. The third section presents (two) aeroacoustic models and the analysis of sound sources based on the FSI simulation. Finally, a short conclusion closes the paper.

2. FSI model

First, the geometrical configuration is showed. Further, the mathematical description of the FSI problem and the FEM discretization procedure is given. Some characteristic results of the flow-induced vibrations of VFs are shown.

2.1. Geometry

The schematic figure of larynx anatomy including VF position without an airways space is shown at Figure 2 followed by a considered idealized two-dimensional geometrical set-up of the FSI problem. For the description of the elastic structure deformation the reference coordinates are utilized, i.e. computational domain $\Omega^s = \Omega_t^s = \Omega_{\text{ref}}^s \subset \mathbb{R}^2$ at arbitrary time t is used. In the case of fluid flow we distinguish between the reference fluid domain $\Omega_{\text{ref}}^f \subset \mathbb{R}^2$, i.e. the domain occupied by fluid at time instant $t = 0$ with the common interface $\Gamma_{\text{W}_{\text{ref}}} = \Gamma_{\text{W}_0}$, and the domain $\Omega_t^f \subset \mathbb{R}^2$ occupied by fluid at any time instant $t \in (0, T)$, which is determined by the motion of the elastic structure (particularly by the position of the interface Γ_{W_t}).

2.2. Mathematical model

We start with the description of the ALE method which allow us to treat relatively easy time-dependency of fluid domain Ω_t^f .

ALE method. This method is based on a diffeomorphic and smooth mapping A_t of any reference point $X \in \Omega_{ref}^f$ on the point of deformed domain $x = A_t(X) \in \Omega_t^f$, particularly the interface can only evolve in time (according to the structural displacement) as $\Gamma_{W_t} = A_t(\Gamma_{W_{ref}})$, while the other boundaries remain static $A_t(\partial\Omega_{ref}^f \setminus \Gamma_{W_{ref}}) = \partial\Omega_{ref}^f \setminus \Gamma_{W_{ref}}$. Further, the ALE domain velocity \mathbf{w}_D representing the velocity of a point x with a given reference $X \in \Omega_{ref}^f$ is defined by

$$\mathbf{w}_D(x, t) = \hat{\mathbf{w}}_D(A_t^{-1}(x), t), \quad \text{where } x = A_t(X) \in \Omega_t^f, \quad (1)$$

and $\hat{\mathbf{w}}_D(X, t) = \frac{\partial}{\partial t} A_t(X)$, for $t \in (0, T)$ and $X \in \Omega_{ref}^f$. Finally, the ALE derivative, i.e. the time derivative with respect to a fixed reference $X \in \Omega_{ref}^f$, satisfies (see [2])

$$\frac{D^A}{Dt} f(x, t) = \frac{\partial f}{\partial t}(x, t) + \mathbf{w}_D(x, t) \cdot \nabla f(x, t). \quad (2)$$

Fluid flow. The flow of a viscous incompressible fluid in the time-dependent domain Ω_t^f is modelled using the Navier-Stokes equations in the ALE form (for details see [2])

$$\frac{D^A \mathbf{v}}{Dt} + ((\mathbf{v} - \mathbf{w}_D) \cdot \nabla) \mathbf{v} - \nu^f \Delta \mathbf{v} + \nabla p = \mathbf{0}, \quad \text{div } \mathbf{v} = 0 \quad \text{in } \Omega_t^f, \quad (3)$$

where $\mathbf{v}(x, t)$ is the fluid velocity, p denotes the kinematic pressure and ν^f is the kinematic fluid viscosity.

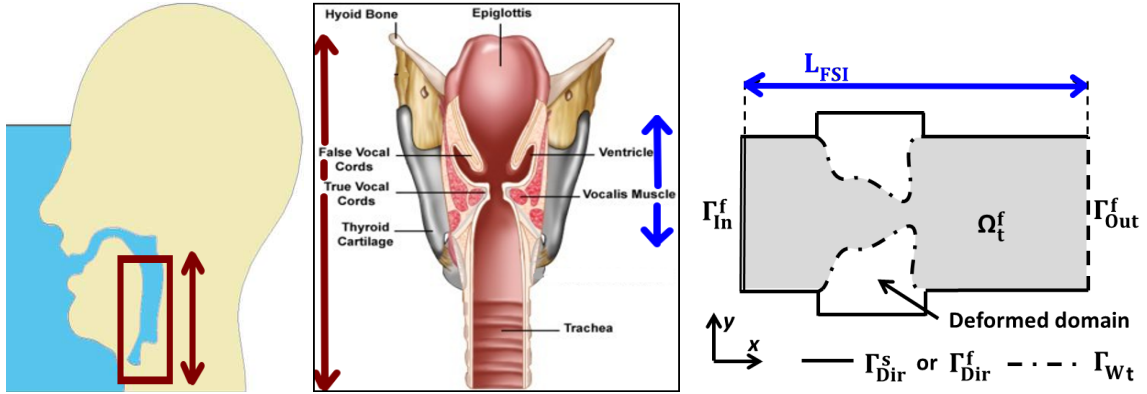


Figure 2: **Left:** Schematic picture of upper human airways. **Middle:** Frontal cut of the larynx reveals the position and a complicated physiological structure of VFs. Arrows denotes approximate scaling with respect to the left and to the right figure. **Right:** Considered simplified FSI geometry undergoing a VFs deformation and the marked boundaries are: inlet Γ_{In}^f , outlet Γ_{Out}^f , walls Γ_{Dir}^f , Γ_{Dir}^s and interface Γ_{W_t} .

We impose the zero initial condition and the following boundary conditions (BCs) alongside equations (3)

$$\begin{aligned}
\text{a)} \quad & \mathbf{v}(x, t) = \mathbf{w}_D(x, t) && \text{for } x \in \Gamma_{\text{Dir}}^f \cup \Gamma_{\text{W}_t}, \\
\text{b)} \quad & (p - p_{\text{ref}})\mathbf{n}^f - \nu^f \frac{\partial \mathbf{v}}{\partial \mathbf{n}^f} = -\frac{1}{2}\mathbf{v}(\mathbf{v} \cdot \mathbf{n}^f)^- && \text{on } \Gamma_{\text{Out}}^f, \\
\text{c)} \quad & (p - p_{\text{ref}})\mathbf{n}^f - \nu^f \frac{\partial \mathbf{v}}{\partial \mathbf{n}^f} = -\frac{1}{2}\mathbf{v}(\mathbf{v} \cdot \mathbf{n}^f)^- + \frac{1}{\epsilon}(\mathbf{v} - \mathbf{v}_{\text{in}}) && \text{on } \Gamma_{\text{In}}^f,
\end{aligned} \tag{4}$$

where the vector $\mathbf{n}^f = (n_j^f)$ denotes the outward unit normal to the boundary $\partial\Omega^f$, p_{ref} denotes a reference pressure and by $(\alpha)^-$ the negative part of real number $\alpha \in \mathbb{R}$ is denoted, i.e. $(\alpha)^- = \min\{0, \alpha\}$. Condition (4 b) is the so-called directional do-nothing boundary condition, which increases the stability in the case of a backward inlet through the outlet boundary, see [11]. Condition (4 c) is the penalization inlet boundary condition, a generalization of the Dirichlet (for $\epsilon \rightarrow 0$) and the Neumann BC (for $\epsilon \rightarrow +\infty$), see [21]. For suitably chosen penalization parameter ϵ its behaviour is favourable, as it allows maintaining the maximal subglottic pressure within a physiological range during the channel closing phase, [16, 21].

Elastic structure. The structure deformation represented by displacement $\mathbf{u}(X, t) = (u_1, u_2)$ of any point $X \in \Omega^s$ is described by partial differential equations

$$\rho^s \frac{\partial^2 u_i}{\partial t^2} - \frac{\partial \tau_{ij}^s}{\partial X_j} = 0, \quad \text{in } \Omega^s \times (0, T), \quad (i = 1, 2), \tag{5}$$

where ρ^s is the structure density and τ_{ij} are the components of the Cauchy stress tensor. The stress tensor components assuming the isotropic body can be expressed as

$$\tau_{ij}^s = \lambda^s \text{div } \mathbf{u} \delta_{ij} + 2\mu^s e_{ij}^s(\mathbf{u}), \tag{6}$$

where δ_{ij} denotes Kronecker's delta and $e_{ij}^s(\mathbf{u}) = \frac{1}{2} \left(\frac{\partial u_j}{\partial X_i} + \frac{\partial u_i}{\partial X_j} \right)$ is the small strain tensor. Parameters λ^s, μ^s are the Lamé coefficients, see e.g. [2]. Problem (5) is equipped with the zero initial conditions and the following BCs

$$\begin{aligned}
\text{a)} \quad & \mathbf{u}(X, t) = \mathbf{u}_{\text{Dir}}(X, t) && \text{for } X \in \Gamma_{\text{Dir}}^s, \\
\text{b)} \quad & \tau_{ij}^s(X, t) n_j^s(X) = q_i^s(X, t), && \text{for } X \in \Gamma_{\text{W}_{\text{ref}}}^s,
\end{aligned} \tag{7}$$

where the $\Gamma_{\text{W}_{\text{ref}}}^s, \Gamma_{\text{Dir}}^s$ are disjoint parts of the boundary $\partial\Omega^s$ and $n_j^s(X)$ are the components of the outward unit normal to $\partial\Omega^s$, see Figure 2.

Coupling conditions. The fluid and structure problems are coupled together with the aid of the interface boundary conditions prescribed at the interface Γ_{W_t} whose position is unknown and it is determined implicitly through the structural displacement \mathbf{u}

$$\Gamma_{\text{W}_t} = \{x \in \mathbb{R}^2 \mid x = X + \mathbf{u}(X, t), X \in \Gamma_{\text{W}_{\text{ref}}}^s\}, \forall t \in (0, T). \tag{8}$$

Further, the kinematic BC representing continuity of velocities across the interface is prescribed for the fluid flow problem in the form of equation (4 a).

The dynamic BC enforcing stress continuity in normal direction at the interface $\Gamma_{\text{W}_{\text{ref}}}$ has the form of equation (7 b), where the components q_i^s of the vector of acting aerodynamic forces \mathbf{q}^s are given by

$$q_i^s = \sum_{j=1}^2 \rho^f \left(p \delta_{ij} - \nu^f \left(\frac{\partial v_i}{\partial x_j} + \frac{\partial v_j}{\partial x_i} \right) \right) n_j^f(x). \quad (9)$$

2.3. Numerical approximation

The FEM is used for spatial discretization of considered subproblems (5) and (3). For the purpose of time discretization the time interval $[0, T]$ is divided into N equidistant parts of length Δt , i.e. $t_n = n\Delta t$, $\Delta t = \frac{T}{N}$, where $n = \{0, 1, \dots, N\}$.

Elastic structure. The FEM discretization of elasticity problem (5) is standard and it leads to the system of ordinary differential equations of the second order

$$\mathbb{M}\ddot{\boldsymbol{\alpha}} + \mathbb{C}\dot{\boldsymbol{\alpha}} + \mathbb{K}\boldsymbol{\alpha} = \mathbf{b}(t), \quad (10)$$

for definitions and further details see [21]. The system (10) is then numerically solved by the Newmark method.

Fluid flow. First, the ALE derivative is discretized by the backward difference formula of second order (BDF2), see [2].

In order to formulate problem (3) weakly, we start with the definition of function spaces involved. The function space for velocity test functions $\mathbf{X} = X \times X$ is defined as follows $X = \{f \in H^1(\Omega^f) \mid f = 0 \text{ on } \Gamma_{\text{Dir}}^f \cup \Gamma_{\text{W}_{t_{n+1}}}^f\}$ and $M = L^2(\Omega^f)$. Then the fluid flow problem can be formulated abstractly in weak form as searching for unknown $V = (\mathbf{v}, p) \in \mathbf{H}^1(\Omega^f) \times M$, which approximately satisfies boundary condition (4a) and

$$a(V, \Phi) + c(V; V, \Phi) + \frac{1}{2}((\mathbf{v} \cdot \mathbf{n})^+ \mathbf{v}, \boldsymbol{\varphi})_{\Gamma_{\text{In}}^f} + \frac{1}{\epsilon}(\mathbf{v}, \boldsymbol{\varphi})_{\Gamma_{\text{In}}^f} = f(\Phi) + \frac{1}{\epsilon}(\mathbf{v}_{\text{Dir}}, \boldsymbol{\varphi})_{\Gamma_{\text{In}}^f} \quad (11)$$

is fulfilled for any test function $\Phi = (\boldsymbol{\varphi}, q) \in \mathbf{X} \times M$, where

$$\begin{aligned} a(V, \Phi) &= \left(\frac{3\mathbf{v}}{2\Delta t}, \boldsymbol{\varphi} \right)_{\Omega^f} + \nu^f (\nabla \mathbf{v}, \nabla \boldsymbol{\varphi})_{\Omega^f} - (p, \text{div } \boldsymbol{\varphi})_{\Omega^f} + (q, \text{div } \mathbf{v})_{\Omega^f}, \\ c(V^*; V, \Phi) &= \frac{1}{2} \left((((\mathbf{v}^* - 2\mathbf{w}_D) \cdot \nabla) \mathbf{v}, \boldsymbol{\varphi})_{\Omega^f} - ((\mathbf{v}^* \cdot \nabla) \boldsymbol{\varphi}, \mathbf{v})_{\Omega^f} + ((\mathbf{v}^* \cdot \mathbf{n})^+ \mathbf{v}, \boldsymbol{\varphi})_{\Gamma_{\text{Out}}^f} \right), \\ f(\Phi) &= \frac{1}{2\Delta t} (4\bar{\mathbf{v}}^n - \bar{\mathbf{v}}^{n-1}, \boldsymbol{\varphi})_{\Omega^f}, \end{aligned} \quad (12)$$

and by $(\alpha)^+$ the positive part of real number $\alpha \in \mathbb{R}$ is denoted, i.e. $(\alpha)^+ = \max\{0, \alpha\}$. The bilinear form $a(\cdot, \cdot)$ and functional $f(\cdot)$ is the standard weak formulation of

Stokes problem. The trilinear form $c(\cdot; \cdot, \cdot)$ represents the skew-symmetric form of the convection, which gives us the directional do-nothing BC (4b), see [11]. The realization of penalization inlet BC (4c) introduces additional terms $\frac{1}{2}((\mathbf{v} \cdot \mathbf{n})^+ \mathbf{v}, \boldsymbol{\varphi})_{\Gamma_{\text{In}}^f} + \frac{1}{\epsilon}(\mathbf{v}, \boldsymbol{\varphi})_{\Gamma_{\text{In}}^f}$ and $\frac{1}{\epsilon}(\mathbf{v}_{\text{Dir}}, \boldsymbol{\varphi})_{\Gamma_{\text{In}}^f}$ in the weakly formulated fluid flow problem, see [21].

The derived weak formulation (12) is discretized by the stabilized FEM, see [21].

Finally, the strongly coupled partitioned approach is selected for the FSI numerical solution, i.e. the convergence of aerodynamic forces in each inner iteration cycle is checked and the fluid flow and the elasticity approximative solutions are iterated in every time step until the difference of aerodynamic forces is smaller than 10^{-5} , see [21].

2.4. Numerical results of the FSI problems

In this part the FSI problem is solved in the full channel with vocal fold model MALE having parabolic shape, see e.g. [5, 16]. All material parameters are the same as in [21, 19], particularly the initial gap is set to $g_{\text{init}} = 0.8 \text{ mm}$ and time step $\Delta t = 2.5 \cdot 10^{-5} \text{ s}$. Then four cases with different inlet BCs are compared:

- 1) case DIR: the Dirichlet boundary condition $\mathbf{v} = \mathbf{v}_{\text{Dir}}$ with the given constant inlet velocity $\mathbf{v}_{\text{Dir}} = (2.1, 0) \text{ m/s}$.
- 2) case PRES: the pressure difference (between the inlet and the outlet) in the form of $p_{\text{ref}} = 400 \text{ Pa}$ is prescribed in condition (4b) on the inlet Γ_{In}^f . The choice of pressure drop ensures that the airflow rates in cases PRES and DIR are comparable.
- 3) case PEN-W: the penalization BC (4c) is applied with the given velocity \mathbf{v}_{Dir} and the penalization parameter $\epsilon = 5 \cdot 10^{-4} \text{ s/m}$.
- 4) case PEN-S: the penalization BC (4c) is applied with the given velocity \mathbf{v}_{Dir} and the penalization parameter $\epsilon = 1 \cdot 10^{-5} \text{ s/m}$.

First, two snapshots from the PEN-S simulation are shown in Figures 3 and 4, illustrating the typical change in VFs position as it alternates between convergent and divergent states. Further, the increasing intensity of glottal jet during opening phase followed by intensity fading for fully open glottis and again the rise of fluid velocity at the glottis up to the maximal values during VF closing phase can be observed. The large vortices formed downstream from the glottis (only the first one is visible in the snapshots) are slowly decaying into smaller ones. The very similar character of the flow field was obtained e.g. in [8].

The given selection of \mathbf{v}_{Dir} and p_{ref} is above critical one and it leads in all cases to flutter instability phenomenon, simulations were terminated by a solver failure due too large structure vibration amplitudes and therefore too much deformed computational fluid mesh. Such behaviour is here documented by the inlet flow velocity, the pressure drop and the (whole) gap width displayed in Figures 5 and 6. We can notice that the inlet velocity is either constant or heavily oscillating in cases of DIR and PRES, respectively. Similarly the pressure drop - if prescribed - remains almost constant, while for the DIR case it grows fast to unphysically high values. This

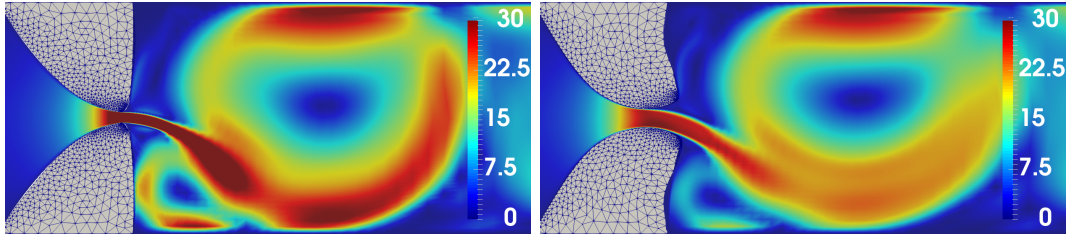


Figure 3: Airflow velocity magnitude in *PEN-S* case at moments of the most closed and the most opened channel. The domain Ω_t^f is in figures truncated.

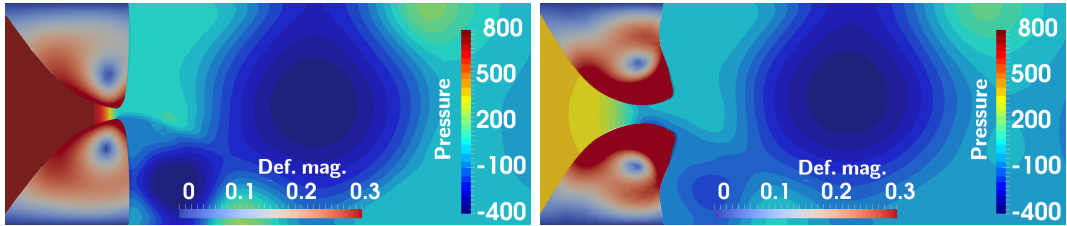


Figure 4: Airflow pressure and magnitude of the VF displacement in mm shown in *PEN-S* case as in Fig. 3.

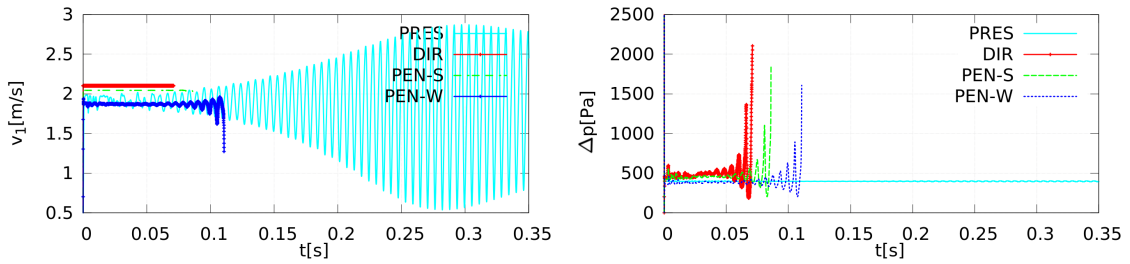


Figure 5: The inlet airflow velocity (left) and pressure difference between the inlet and the outlet of the channel (right) for cases *DIR*, *PEN-S*, *PEN-W* and *PRES*.

behaviour is expected as theoretically the pressure drop in the *DIR* case would reach infinity as the channel approaching closure.

The behaviour of the *PEN-S* and *PEN-W* cases, i.e. a generalization of both previous BCs with switching controlled by parameter ϵ , provides a combination of the aforementioned. The inlet velocity can a little oscillate and the pressure drop gradually rises as the gap between VFs starts to close more and more, see Figure 6. Nevertheless, the maximal value of the pressure drop is obviously controlled by the value of ϵ .

Further, the VF vibration pattern can be illustrated on the phase portraits of point S (the top point of the bottom VF), see Figure 7. The phase portraits of cases *DIR* and *PEN-S* indicate a much faster development of the flutter phenomenon than in case *PRES*. The phase portrait of case *PRES* moreover differs in the motion of point S, the different motion pattern(s) is evidently excited.

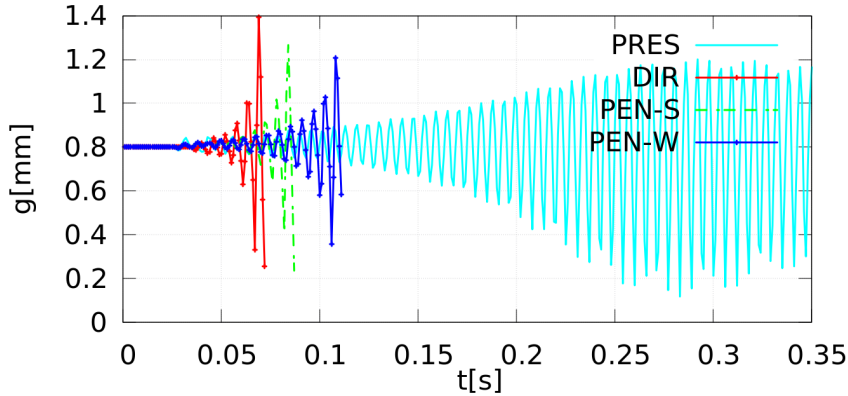


Figure 6: Time development of the gap in cases *DIR*, *PEN-S*, *PEN-W* and *PRES*.

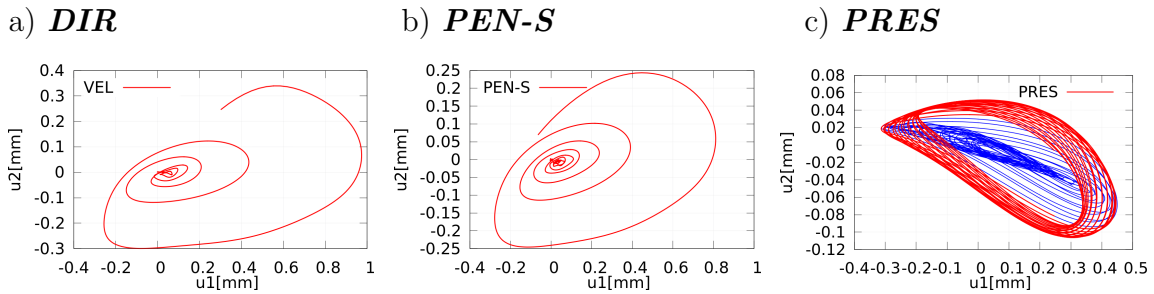


Figure 7: Trajectory of point S in the X–Y plane. The blue curve in the *PRES* case shows the initial development, while the red one marks the developed VF vibrations.

Additionally, the dependence of the transglottal pressure on the gap can be constructed from Figures 5 and 6 by time elimination, see Figure 8. The pressure-gap curve is a rough estimate of the transferred energy from airflow to VF vibration provided by means of an area A closed inside, [4], and it is usually a good metric in the case of laboratory experiments, although the transferred energy can be precisely computed for the case of numerical simulation, see e.g. [19].

The pressure-gap curves in Fig. 8 capture the flutter regime and they are not closed as the regular periodic VF vibration cycle has not emerged yet (typically connected with VF mutual contact). Nevertheless, it is obvious that the pressure drop associated with reaching a certain minimal gap value is much lower for case *PEN-S* (and also for *PEN-W*) compared to the *DIR* case, and it still remains within the physiological range, i.e. below circa 3 kPa, [17]. The orientation of the curves in all cases is anticlockwise, which is interestingly in a contradiction with laboratory results of [4].

3. Aeroacoustic models

First, the considered two-dimensional geometry is shown. Then two different aeroacoustic analogies are described. Finally, the acoustic sources and corresponding results of simplified FSAI simulation are shown.

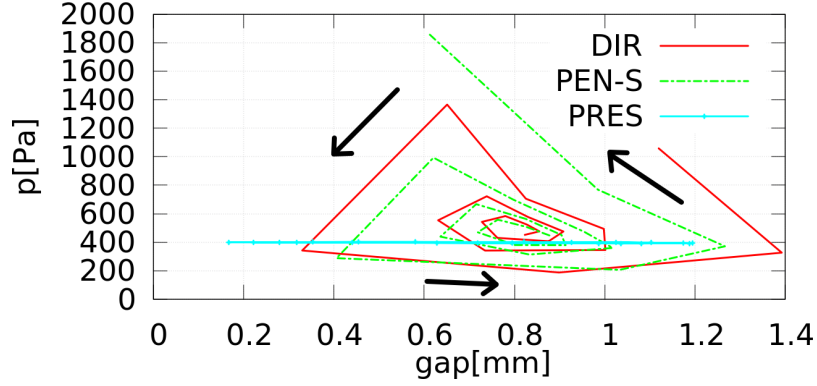


Figure 8: Dependence of the transglottal pressure on the gap for three simulations of the FSI problem: *DIR*, *PEN-S* and *PRES*. The graph depicts only last four incomplete oscillation cycles and it is undulated due to too low sampling rate of the data saving. Arrows show the orientation of the curves (i.e. time progression).

3.1. Geometry configuration

The acoustic domain Ω^a , where the acoustic problem is solved, is depicted in Figure 9, compare it with Figure 2. It is composed of three parts, i.e. $\Omega^a = \overline{\Omega_{\text{src}}^a} \cup \overline{\Omega_{\text{air}}^a} \cup \overline{\Omega_{\text{pml}}^a}$. The acoustic sources are calculated from the known flow field exclusively in the domain Ω_{src}^a , which is the same as the reference fluid domain, i.e. $\Omega_{\text{src}}^a = \Omega_{\text{ref}}^f$.¹ The domain Ω_{air}^a represents a part of the vocal tract behind the glottis up to the mouth (indicated by arrow L_{tract} in Fig. 9) including a far field region (arrow L_{free}), i.e. the outer space. The PML domain Ω_{pml}^a (see arrow L_{PML}) closes both the aforementioned domains in order to damp the outgoing sound waves.

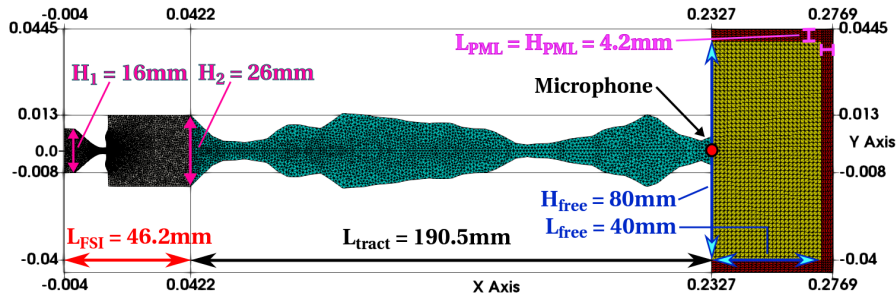


Figure 9: Computational acoustic domain Ω^a with vocal tract model M1 described later and its dimensions. Microphone is placed in the mouth opening.

3.2. Mathematical models of the aeroacoustic problem

Aeroacoustics studies sound generated by aerodynamic processes, typically sound generated by flow around obstacles or by turbulence, see e.g. [7], [1]. The compress-

¹The change of domain Ω_{src}^a in time is neglected. Sound sources outside domain Ω_{src}^a are omitted.

ible Navier-Stokes equations in general describe all aspects of fluid flow including acoustics. However, acoustic pressure is usually a tiny part of the total pressure, often comparable to numerical errors. Additional challenges arise from length scale disparities or unwanted dispersion and dissipation properties of numerical schemes, see [7]. To address these challenges, hybrid acoustic analogies, which decouple fluid flow and acoustic problems, provide an effective and practical solution by allowing the use of problem-specific solvers.

3.2.1. Lighthill acoustic analogy

The Lighthill analogy was derived from compressible Navier-Stokes equations under the assumption that acoustic waves with origin in a small source region propagate through a surrounding medium in rest state characterized by $\mathbf{v}_0 = \mathbf{0}$, p_0 and rest fluid density ρ_0^f . The Lighthill analogy has the final form of inhomogenous wave equation for unknown pressure fluctuation $p' = p - p_0$

$$\frac{1}{c_0^2} \frac{\partial^2 p'}{\partial t^2} - \frac{\partial^2 p'}{\partial x_i^2} = \frac{\partial^2 T_{ij}}{\partial x_i \partial x_j}, \quad (13)$$

with a given speed of sound c_0 and known values of the Lighthill tensor $\mathbf{T} = (T_{ij})$, which double divergence plays role of effective sound source term. The components of the Lighthill tensor T_{ij} are given by

$$T_{ij} = \rho^f v_i v_j + ((p - p_0) - c_0^2(\rho^f - \rho_0^f))\delta_{ij} - \tau_{ij}^f \approx \rho_0^f v_i v_j, \quad (14)$$

where τ_{ij}^f is the fluid viscous stress tensor and the subsequent approximation of the Lighthill tensor by neglecting the viscous stress τ_{ij}^f and the stresses connected with the non-isentropic processes $(p' - c^2 \rho')\delta_{ij}$ are applied according to [9], [1].

The disadvantage of the Lighthill analogy is that pressure fluctuation p' can be regarded as the acoustic pressure p^a only outside the flow domain because inside the source region it represents a superposition of acoustic and hydrodynamic pressures, see [7], [1].

3.2.2. Perturbed convective wave equation

Another suitable choice from many other acoustic analogies is the PCWE, see [6, 7]. Its aim is to describe more precisely the behaviour of purely acoustic components. It is based on splitting of physical quantities into mean and fluctuating parts. The fluctuating variables consists of acoustic parts \mathbf{v}^a , p^a and non-acoustic components \mathbf{v}^{ic} , p^{ic} , (i.e. incompressible parts)

$$p = \bar{p} + p^{ic} + p^a, \quad \mathbf{v} = \bar{\mathbf{v}} + \mathbf{v}^{ic} + \mathbf{v}^a, \quad (15)$$

see [7]. Assuming incompressible homoentropic flow the splitting leads to the following partial differential equation for unknown \mathbf{v}^a and p^a

$$\frac{\partial p^a}{\partial t} + \bar{\mathbf{v}} \cdot \nabla p^a + \rho_0^f c_0^2 \nabla \cdot \mathbf{v}^a = -\frac{Dp^{ic}}{Dt}, \quad \frac{\partial \mathbf{v}^a}{\partial t} + \nabla(\bar{\mathbf{v}} \cdot \mathbf{v}^a) + \frac{1}{\rho_0^f} \nabla p^a = \mathbf{0}, \quad (16)$$

where the substantial derivative $\frac{D}{Dt}$ equals $\frac{D}{Dt} = \frac{\partial}{\partial t} + \bar{\mathbf{v}} \cdot \nabla$. These equations can be rewritten into scalar one, denoted as PCWE, with the help of acoustic potential ψ^a , which is related to the acoustic particle velocity as $\mathbf{v}^a = -\nabla\psi^a$ (since the acoustic velocity field is irrotational)

$$\frac{1}{c_0^2} \frac{D^2\psi^a}{Dt^2} - \Delta\psi^a = -\frac{1}{\rho_0^f c_0^2} \frac{Dp^{ic}}{Dt}. \quad (17)$$

Moreover, for low velocities, we can simplify (17) by disregarding the convection effect and setting $\bar{\mathbf{v}} = 0$, see [18]. A relatively big advantage comparing (17) with (13) is only one and just the time derivative of right hand source term. The numerical computation of the time derivative is usually less sensitive to numerical errors, [7, 1], and also it is usually well resolved in time.

The equations (13) or (17) are equipped with the zero initial conditions and the boundary of acoustic domain $\partial\Omega^a$ with the outer normal \mathbf{n}^a is considered as fully reflecting (called also sound hard)

$$\frac{\partial P}{\partial \mathbf{n}^a}(x, t) = 0 \quad \text{for } x \in \partial\Omega^a, t \in (0, T), \quad (18)$$

where P denotes the appropriate acoustic unknown.

PML. In order to mimic the open-boundary problem of radiation acoustic waves outside the human head the PML technique is used. The key of this technique is to add a new PML subdomain on the boundary. The proper choice of complex values of sound speed and density governed by the set of artificial equations inside the PML domain leads to exponential wave damping inside PML and to eliminating any reflection of acoustic waves on the interface between the propagation domain and the PML. We further refer to [7].

3.3. Numerical approximation

For the numerical solution the FEM is again used, see e.g. [18]. The interpolation of aeroacoustic sources from the computational fluid to the acoustic mesh is performed with the help of the program CFSDat, see [7].

3.4. Numerical results of the simplified FSAI problem

This part contains acoustic results corresponding to proper choice of acoustic domains characterized by their resonant frequencies, computation and analysis of sound sources and finally the transient computation providing the frequency spectra of phonation of vowel [u:].

3.4.1. Resonant frequencies of acoustic domains

Two variants of acoustic domain Ω^a are analyzed here in order to find their acoustic resonant frequencies, usually called formants. In both cases the acoustic domains

differ only in the portion of inclusion of domain Ω_{src}^a . The first variant is labeled as M1 (model 1) and the second as M2 (model 2), which has removed the subglottal and the glottal regions, see Figure 10. The part of domain Ω^a representing the VT model for the vowel [u:] based on vocal tract cross-section MRI segmentation [14] is for M1 and M2 models the same, see Figure 9 and [22].

The formants of vocal tract are determined by the transfer function approach due to inclusion of the PML layer prohibiting a natural choice of modal analysis. In this approach, the ratio of the output to the input (unit) signal \hat{F} is evaluated based on the Helmholtz equation (wave equation in frequency domain), see [7, 22],

$$-\left(\frac{\omega^2}{c_0^2} + \Delta\right) \hat{p} = \hat{F}, \quad (19)$$

where the speed of sound $c_0 = 343$ m/s, ω denotes the angular frequency and $\hat{p}(x, \omega)$ is the Fourier transform of $p(x, t)$. As output is regarded \hat{p} at the microphone position in the investigated frequency range 50 – 3000 Hz.

The transfer functions computed for models M1 and M2 are shown in Figure 10 on the right and the found formants are listed in Table 1. Both models M1 and M2 have four formants in the range 50 – 2500 Hz, M1 having an additional formant F5 at 2638 Hz due to the subglottal part of the VT model, see [22]. The occurrence of F3 at frequency 1432 Hz contrary to Story’s results [14] is probably caused by the longer acoustic domain (the length of approx. 23 cm compared to Story’s length of 18.25 cm). The formant frequency F4 of both models lies in the vicinity of Story’s reference F3, however the M2 model is chosen for further simulations due to a higher similarity with results of [14].

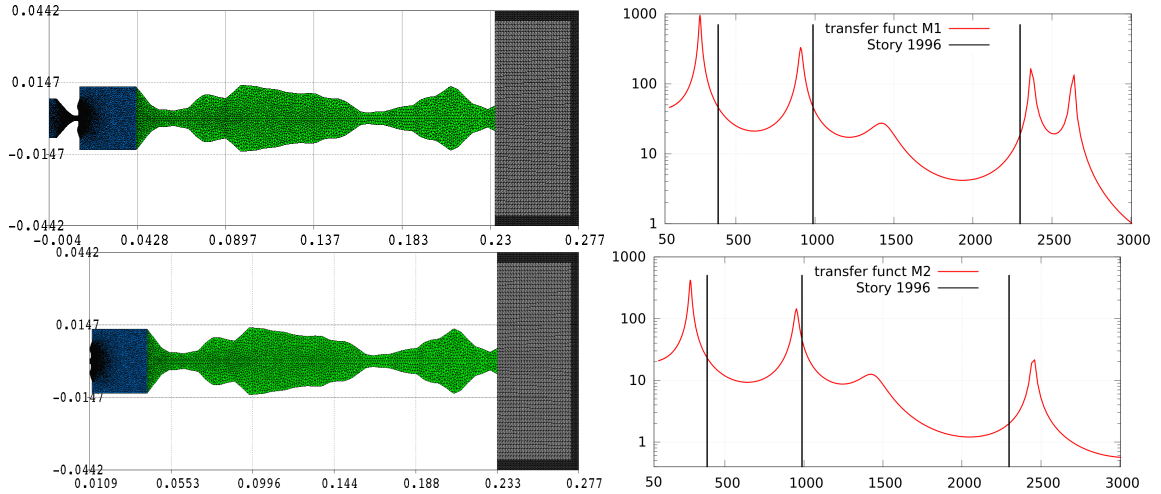


Figure 10: **Left:** Acoustic models M1 and M2. **Right:** Computed transfer functions for given cases. The formants of vowel [u:] from [14] are highlighted by vertical lines.

	F_1	F_2	F_3	F_4
M1	271	909	1432	2365
M2	280	952	1432	2440
Story	389	987	2299	–

Table 1: Computed formant frequencies (in Hz) of the vocal tract models M1 and M2. The measured (Story) results for vowel [u:] are from reference [14].

3.4.2. Sound sources

The aeroacoustic results are based on the FSI results obtained with four-layered VF of shape denoted by us as ZORNER and inlet pressure difference of 800 Pa, see the detailed settings and the results of fluid flow in [18]. The sound sources computed from the FSI results are analyzed to get a spatial distribution and frequency content. Finally, the sound source propagation in the chosen acoustic model M2 of both aeroacoustic approaches – LH and PCWE, are compared.

Spatial distribution of sound sources for different aeroacoustic approaches.

The sound sources computed for both different approaches according to (14) and (17) are displayed in Figure 11. In the LH case the sound sources are primarily associated with the velocity gradients and in the current simulation they are greatly distributed downstream of the glottis, where the glottal jet creates strong shear layers as it enters the supraglottal spaces, and also in the vicinity of the VF boundary, where the glottal jet separates from the VF surface.

The dominant sound sources in the cases of the PCWE approach are connected with pressure time changes, which local extremes are located primarily in the vortex centers. The vortices are formed by a complex decay of the glottal jet downstream the glottis. The sound source structure is similar as in phase-locked PIV measurements [10] or in the numerical simulations [12].

Frequency content. The frequency content of the sound sources is investigated with the Fourier transform applied on the time signal at each point of the sound sources. The power spectral densities (PSD) of the sound sources at two representative frequencies for both aeroacoustic approaches are shown in Figure 12. The frequencies 232 Hz and 2486 Hz are the local spectral maxima representing one of the dominant VF vibration frequencies and an (higher) non-harmonic frequency, respectively. The quantitative comparison of sound sources PSD values is here irrelevant as in all cases a different acoustic quantity is depicted.

The location of main sound sources for frequency 232 Hz for all considered cases is inside the glottis and having dipole character. The LH sources located before the tip of VFs are less prominent than the quadrupole-like structure formed downstream from the narrowest part of the channel. In the PCWE case the dipole clearly dominates. These findings coincide very well with the results of [13].

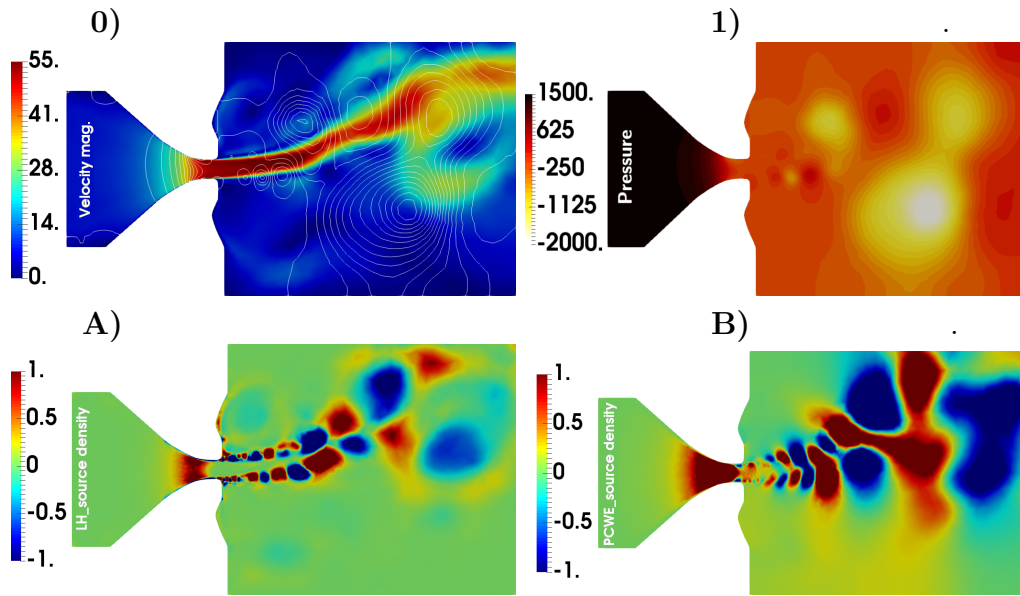


Figure 11: Comparison of (normalized) instant sound densities for different aeroacoustic approaches at chosen time instant shown together with the flow field. **0)** The magnitude of airflow velocity. **1)** The pressure distribution. Below instant sound densities are shown for: **A)** the LH analogy and **B)** the PCWE approach.

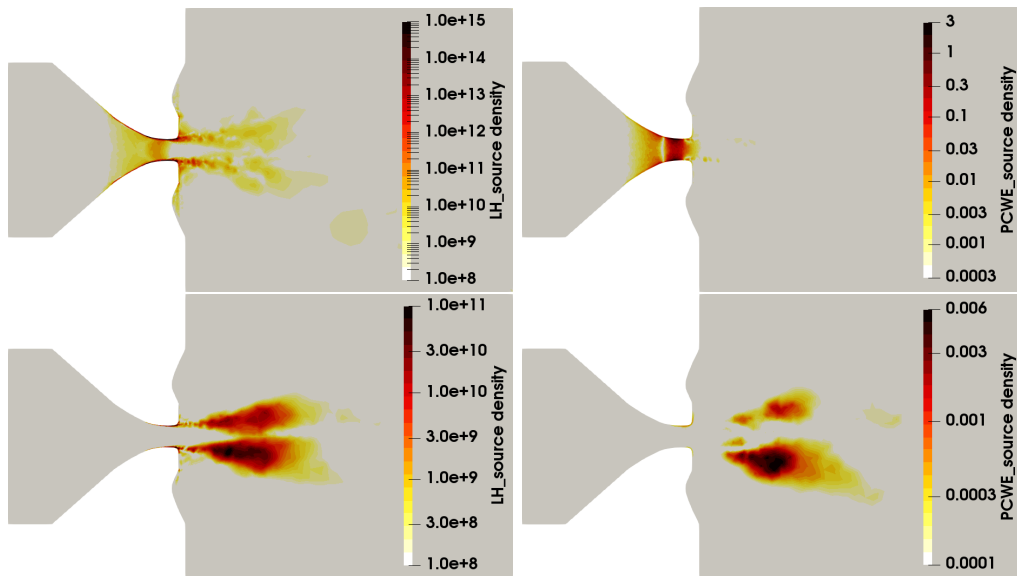


Figure 12: Computed power spectral densities of sound sources at **232 Hz** (top) and **2486 Hz** (bottom) for the LH (left) and PCWE approach (right). The color scale is logarithmic, and it is different for each figure.

The higher frequency sources like e.g. at 2486 Hz are mainly located in the supraglottal channel, see Figure 12 bottom. These sound sources can be associated with the free jet pouring out of an opening (glottis). In the LH case the sound sources at 2486 Hz are located along boundaries of the glottal jet, cp. [10]. The PCWE sound sources are situated in the supraglottal area typically following periodic series of vortices centers, nevertheless in this case the PSD graph is dominated by the merged spatial maxima of the first four vortices.

3.4.3. Sound propagation in the chosen acoustic domain

The sound sources of the Lighthill (LH) analogy and the simplified PCWE (sPCWE) approach, where the convection effects are disregarded on the left-hand side of (17) while keeping the full right-hand sound sources of (17), similar as in [18]. The computed sound sources are then used for their time propagation in the chosen acoustic domain M2 and the resulting acoustic pressure is observed in the microphone position. Its sound pressure levels at frequency domain up to 3 kHz are shown in Figure 13. Both approaches detect four frequency peaks matching very well the first four formants of the vocal tract model M2, but there are substantial differences in the SPL maxima. For the LH case the first frequency of 278 Hz reaches the highest SPL of circa 135 dB followed by frequency peaks 942 Hz and 2421 Hz, each gradually lowered by approximately 20 dB. The sPCWE approach is able to predict all four formants with more equal distribution of SPL, where the most significant peak with circa 110 dB is located at the frequency of F_2 contrary to the LH case. This is in agreement with [10] stating clear domination of the first frequency peak of the LH simulation, see also [13] and cf. [12]. Our previous results of [18] were spoiled by a wrong setting of PML contrary to the latest one, see [20, 15].

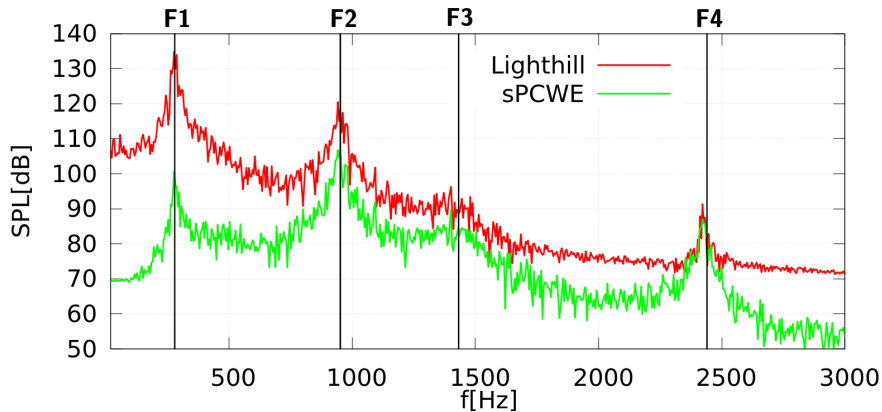


Figure 13: Sound pressure levels of acoustic pressure in the frequency domain, obtained by the LH analogy and the sPCWE approach at the microphone position (see Fig. 9). The black vertical lines mark the formants of acoustic domain M2, see Table 1.

The high values of SPL (comparable to a loud singing) are probably caused, first, by a relatively high prescribed pressure drop and the position of the microphone directly at the mouth opening, cf. [23]. Second, there is a generally different 2D fluid flow dynamics contrary to more complex 3D fluid flow dynamics (having impact on the aerodynamical sound sources). Finally, in agreement with [13], we regard the SPL results of the LH analogy as overestimated due to the absence of acoustic/hydrodynamic splitting, which leads to the superimposition of hydrodynamic quantities in the sound sources.

4. Conclusion

This article presents a complex problem of fluid-structure-acoustic interaction, motivated by human phonation. To simulate normal speech, a suitable approach is to use the fluid-structure interaction model to describe flow-induced VF vibrations as the main phonation mechanism, along with the application of acoustic analogies to separately solve the aeroacoustic problem. The both aforementioned problems are mathematically described and numerically approximated using FEM-based solvers.

The FSI numerical results compare flow characteristics for three inlet boundary conditions, showing that the penalization BC effectively controls maximal pressure difference during the channel closing phase. The simulation of flutter regime is documented by phase portraits of the selected point and by the curve plotting the dependence of the transglottal pressure on the gap.

In the acoustic results, the resonant acoustic frequencies of different acoustic domains are first investigated. Then the sound source analysis reveals the major sound source distribution at the glottis for low frequencies connected to VF vibration, while the majority of high-frequency sources is located at the supraglottal area. Finally, the acoustic pressure at the mouth position is obtained by the propagation of sound sources in time. Its SPL shows that the formant frequencies are the most dominant ones, as expected for the simulation without VF contact. The results of the Lighthill analogy obviously overestimates SPL, while the sPCWE results seem promising.

Acknowledgements

The work was supported by grant No. SGS24/120/OHK2/3T/12 of CTU in Prague and from Premium Academiae of Prof. Nečasová. This work was supported by the Institute of Mathematics of the Czech Academy of Sciences (RVO:67985840). The authors gratefully acknowledge the Center of Advanced Aerospace Technology (CZ.02.1.01/0.0/0.0/16.019/0000826) at the Czech Technical University in Prague for awarding the access to computing facilities.

References

- [1] Delfs, J.: *Basics of Aeroacoustics*. Technische Universitaet Braunschweig, 2016.
- [2] Feistauer, M., Sváček, P., and Horáček, J.: Numerical simulation of fluid-structure interaction problems with applications to flow in vocal folds. In: T. Bodnár, G.P. Galdi, and S. Nečasová (Eds.), *Fluid-structure Interaction and Biomedical Applications*, Birkhauser, 2014.
- [3] Girault, V. and Raviart, P.A.: *Finite element methods for Navier-Stokes equations*. Springer-Verlag, 1986.
- [4] Horáček, J., Radolf, V., and Laukkanen, A.M.: Experimental and computational modeling of the effects of voice therapy using tubes. *J. Speech Lang. Hear. Res.*, 2019 pp. 1–18.
- [5] Horáček, J., Šidlof, P., and Švec, J.: Numerical simulation of self-oscillations of human vocal folds with Hertz model of impact forces. *J. Fluids Struct.* **20** (2005), 853–869.
- [6] Hüppe, A. and Kaltenbacher, M.: Spectral finite elements for computational aeroacoustics using acoustic perturbation equations. *J. Comput. Acoust.* **20** (2012), 1240 005.
- [7] Kaltenbacher, M.: *Numerical simulation of mechatronic sensors and actuators: finite elements for computational multiphysics*. Springer, 2015.
- [8] Kosík, A., Feistauer, M., Hadrava, M., and Horáček, J.: Numerical simulation of the interaction between a nonlinear elastic structure and compressible flow by the discontinuous Galerkin method. *Appl. Math. Comput.* **267** (2015), 382–396.
- [9] Lighthill, M.J.: On sound generated aerodynamically. I. General theory. In: *Proceedings of the Royal Society of London*, vol. 211. The Royal Society, 1952 pp. 564–587.
- [10] Lodermeier, A. et al.: Aeroacoustic analysis of the human phonation process based on a hybrid acoustic PIV approach. *Experiments in Fluids* **59** (2018).
- [11] Neustupa, T.: Existence of a steady flow through a rotating radial turbine with an arbitrarily large inflow and an artificial boundary condition on the outflow. *J. Appl. Math. Mech.* **103** (2023).
- [12] Schoder, S. et al.: Aeroacoustic sound source characterization of the human voice production-perturbed convective wave equation. *Appl. Sci.* **11** (2021), 2614.

- [13] Šidlof, P., Zörner, S., and Hüppe, A.: A hybrid approach to the computational aeroacoustics of human voice production. *Biomechanics and Modeling in Mechanobiology* **14** (2014), 473–488.
- [14] Story, B. H., Titze, I. R., and Hoffman, E. A.: Vocal tract area functions from magnetic resonance imaging. *JASA* **100** (1996), 537–554.
- [15] Sváček, P. and Valášek, J.: Numerical Simulation of Fluid-Structure-Acoustic Interactions Models of Human Phonation Process. In: Bodnár, T., Galdi, G.P., Nečasová, Š. (Eds.), *Fluids Under Control. Advances in Mathematical Fluid Mechanics*, Birkhäuser, Cham, 2023.
- [16] Sváček, P. and Horáček, J.: Finite element approximation of flow induced vibrations of human vocal folds model: Effects of inflow boundary conditions and the length of subglottal and supraglottal channel on phonation onset. *Appl. Math. Comput.* **319** (2018), 178–194.
- [17] Titze, I. R.: *Principles of voice production*. Prentice Hall, 1994.
- [18] Valášek, J., Kaltenbacher, M., and Sváček, P.: On the application of acoustic analogies in the numerical simulation of human phonation process. *Flow Turbul. Combust.* **102** (2019), 129–143.
- [19] Valášek, J. and Sváček, P.: On aerodynamic force computation in fluid-structure interaction problems - comparison of different approaches. *J. Comput. Appl. Math.* **429** (2023), 115–208.
- [20] Valášek, J. and Sváček, P.: Aeroacoustic simulation of human phonation based on the flow-induced vocal fold vibrations including their contact. *Adv. Eng. Softw.* **194** (2024).
- [21] Valášek, J., Sváček, P., and Horáček, J.: On suitable inlet boundary conditions for fluid-structure interaction problems in a channel. *Applications of Mathematics* **64** (2019), 225–251.
- [22] Valášek, J., Sváček, P., and Horáček, J.: The influence of different geometries of human vocal tract model on resonant frequencies. In: D. Šimurda and T. Bodnár (Eds.), *Topical problems of fluid mechanics 2018*. Institute of Thermomechanics, AS CR, 2018 pp. 307–314.
- [23] Zörner, S. and Kaltenbacher, M.: Fluid-structure-acoustic interaction algorithms and implementations using the finite element method. In: *Eccomas*, Vol. 2010. 2010 p. 28.

